

Supplementary Materials for

Exploration of metastability and hidden phases in correlated electron crystals visualized by femtosecond optical doping and electron crystallography

Tzong-Ru T. Han, Faran Zhou, Christos D. Malliakas, Phillip M. Duxbury, Subhendra D. Mahanti, Mercuri G. Kanatzidis, Chong-Yu Ruan

Published 26 June 2015, *Sci. Adv.* **1**, e1400173 (2015)
DOI: 10.1126/sciadv.1400173

This PDF file includes:

Text

Fig. S1. Optical image of a 45-nm-thick exfoliated single-crystal 1T-TaS₂ sample supported on a standard 1000-mesh gold TEM grid.

Fig. S2. Steady-state and dynamical diffraction patterns of 1T-TaS₂ in the NC-CDW state taken at room temperature.

Fig. S3. The selected CDW patterns under different optical excitation fluences for constructing the optical doping–induced phase diagram obtained at $T_B = 150$ K using the 800-nm femtosecond photons for optical doping.

Fig. S4. The determination of CDW phase boundaries based on the presence of a step or a slope change.

References (50–54)

1. SAMPLE PREPARATION METHODS

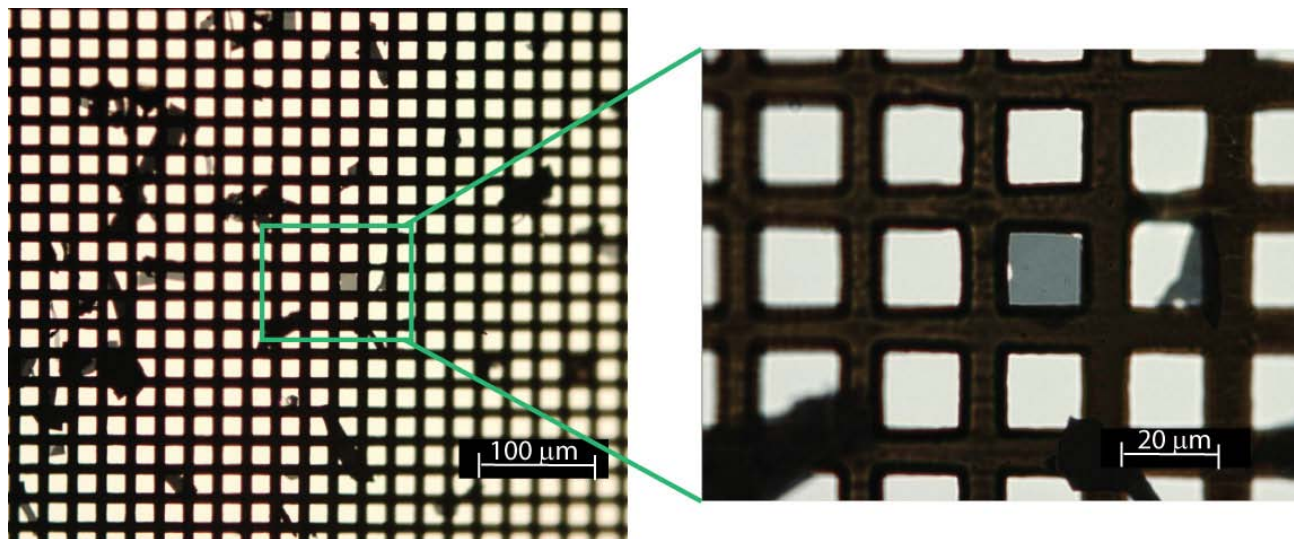


Fig. S1. Optical image of a 45 nm thick exfoliated single-crystal 1T-TaS₂ sample supported on a standard 1000-mesh gold TEM grid.

Single crystals of 1T form of TaS₂ were grown by the chemical vapor transport technique. Pure elements of Ta (1.426 g) and S (0.518 g) were loaded with a 1:2.05 ratio into a fused silica tube (9 mm in diameter and around 24 cm in length) together with a small amount of I₂ (0.068 g). The tube was flame sealed under vacuum ($<10^{-4}$ torr) and placed in a dual zone furnace with a hot zone at 950 °C and a cold zone at 900 °C. The temperature was ramped up in 1 day and the tube was soaked for 2 days at the target temperature. After 1 day of cooling time, single crystals of different sizes were formed on the cold side of the tube [50]. For studies by electron crystallography, 1T-TaS₂ single crystal samples were exfoliated repeatedly by the Scotch tape method [51] down to ~40nm thick. Then the thin samples on Scotch tape were suspended in acetone by submerging the Scotch tape in acetone. Acetone solution containing samples was dropped onto standard TEM grids with a pipette. After the acetone solution evaporated, the sample pieces were left free standing on the grid (see Fig. S1). Sample sizes from the same Scotch tape could vary from one to another, but typically range from 30 to 100 μm in size. The samples chosen in our experiments are 30-50 nm in thickness and ~20 μm in width on the TEM grid. Suitable samples were prescreened from the contrast in optical microscope and then the thickness was determined by performing zero-loss electron energy loss spectroscopy (EELS) thickness map using transmission electron microscopy (TEM).

2. EXPERIMENTAL SETUP

We performed ultrafast electron crystallography (UEC) in an ultrahigh vacuum chamber equipped with a custom-made cryogenic sample goniometer, with temperature control that ranges from 20K to above room temperature. Temperature was measured with 0.01K precision at the back of the sample holder, which was in solid thermal contact with the sample grid, which was clamped into a copper counter sink on the sample holder. The electron gun and experimental set up has been described in detail elsewhere [38]. Briefly, a proximity-coupled cathode-anode-lens assembly was employed to accelerate the photoelectrons to 30keV, then focused and collimated by double apertures to form a beam, all within a short distance of 5 cm from the sample plane. The probe size was controlled via adjusting the focusing strength of the magnetic lens and ranged from 20 to 40 μm in full-width-at-

half-maximum (FWHM) in this experiment ensuring the electron probe beam was fully contained within a single sample flake. The pump pulse was generated by an optical parametric amplifier driven by a 45 fs, 800 nm amplified laser system (Spectra Physics, Ti: Sapphire, Regenerative Amplification), and can be tuned from 200nm to 3000nm in wavelength. In this experiment, wavelengths 800 nm and 2500 nm were used. The size of the pump beam at different wavelengths was adjusted by varying the position of a focusing lens, and characterized via a knife-edge method *in situ*. We set the pump size to be $\sim 400 \mu\text{m}$ in FWHM, which was significantly larger than the sample size to ensure that within the probed area the sample was homogeneously illuminated by the pump laser. We kept the electron counts to be $\sim 500 e^-$ per pulse, yielding an electron pulse-length of 300 fs at FWHM or 150 fs at HWHM, which defined the shortest response time of our experiment [52].

3. DATA ANALYSIS

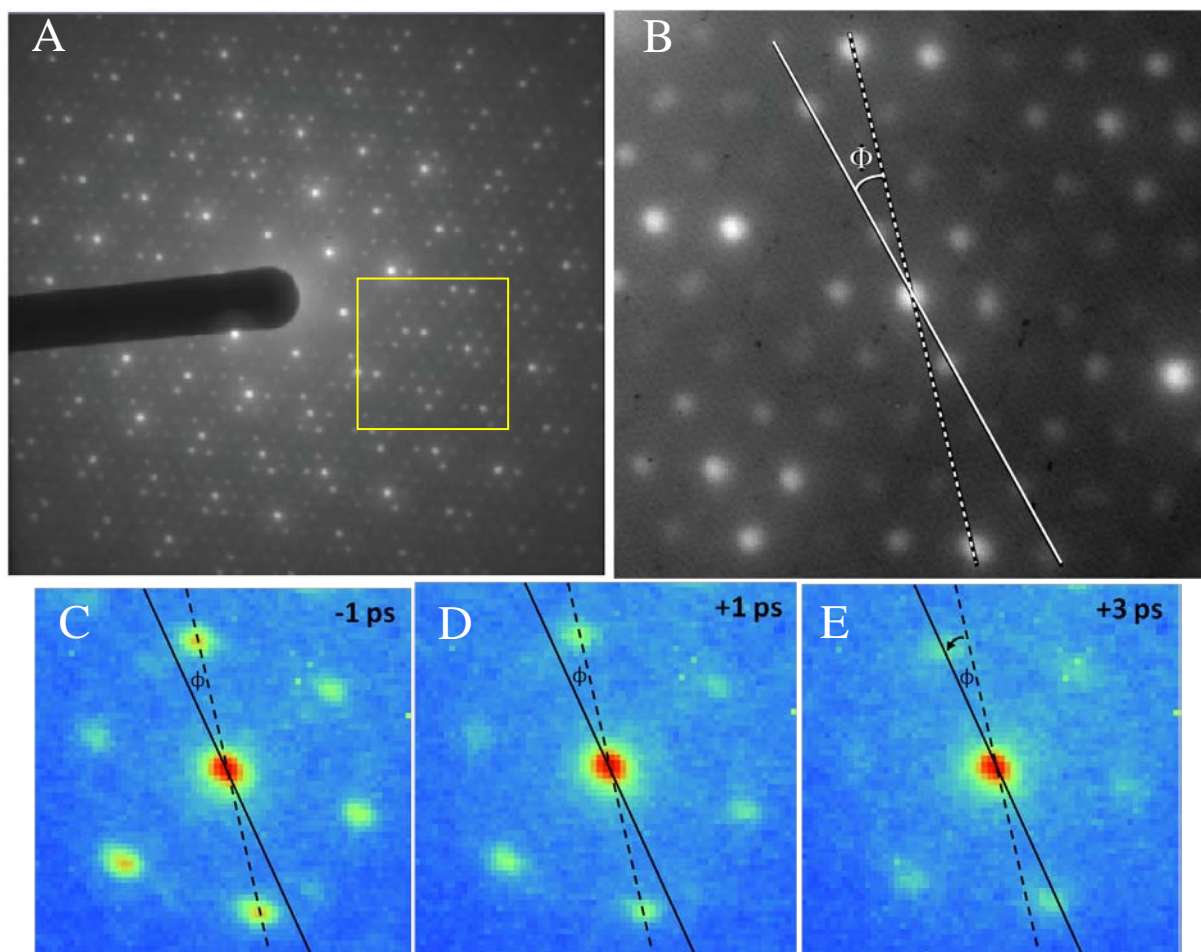


Fig. S2. (A) Diffraction pattern of 1T-TaS₂ in the NC-CDW state taken at room temperature. The image is on a logarithmic scale to make the CDW peaks more visible. (B) Scale-up view of the diffraction pattern from the square region in (A), showing clear hexagonally distributed first-order CDW satellite peaks around the central lattice Bragg peaks. Second-order CDW satellite peaks are also visible. (C-E) Time-dependent diffraction images from a single Bragg peak region at different time delays: -1ps, +1ps, +3ps respectively. The solid line connects neighboring Bragg peaks, representing the direction of the lattice vector \mathbf{G} . The dashed line connects neighboring CDW peaks, representing the direction of the CDW vector \mathbf{Q} . Φ represents the angle between CDW and Bragg vectors. In (E), the CDW vector \mathbf{Q} rotates fully into the lattice vector direction, indicating that the NC-CDW is transformed to IC-CDW by 3 ps after arrival of the pump laser pulse.

In the analysis, we focus on determining the CDW peak intensity and the CDW angle Φ between the CDW wave-vector (\mathbf{Q}) and the lattice vector (\mathbf{G}) (see Fig. S2). To determine Φ , we employ angular line intensity scans along the direction perpendicular to CDW vector \mathbf{Q} crossing the CDW satellite peaks to produce the angular profile of the CDW peaks. The width of the scan is set at twice of the FWHM of the CDW peaks so it covers most of the individual peak intensity but not those from the neighboring peaks. After obtaining the angular profiles, we use Gaussian functions to fit the peaks, and determine the position and intensity associated with each CDW peak precisely. The background is removed by second order polynomial fitting, along with the Gaussian peak fitting. We do the same for Bragg peaks and completely determine the \mathbf{Q} and \mathbf{G} vectors from the diffraction pattern, so Φ can be calculated precisely.

The repetition rate is set to be 1 kHz or lower to ensure full recovery of the system so each pump-probe cycle is independent. In the fluence scans, the time point we chose for the peak intensity change and rotation angle is +20ps, as at this delay time the system reaches a long-lived metastable state at all fluences.

4. CONSTRUCTING THE PHASE DIAGRAM

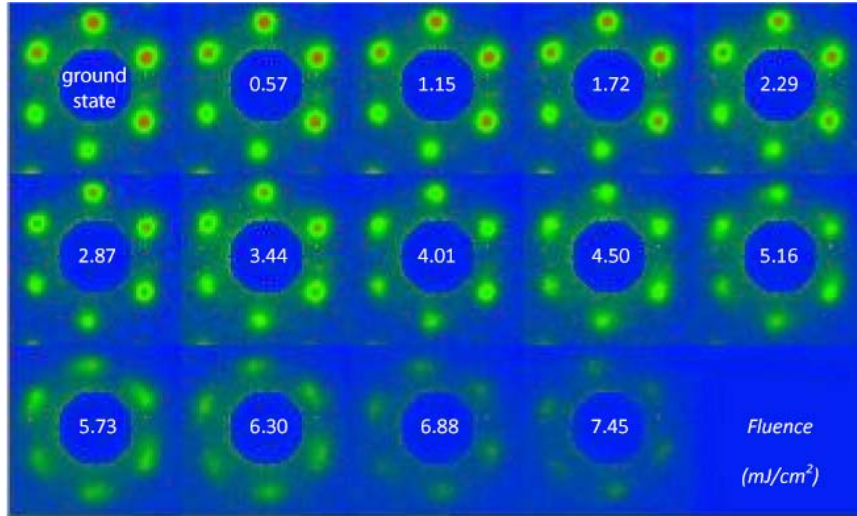


Fig. S3 The selected CDW patterns under different excitation fluences (F) for constructing the optical-doping-induced phase diagram. The data set shown here are obtained at $T_B=150\text{K}$ using the 800nm fs photons for optical doping. The central Bragg peak is masked out to highlight the CDW satellite peaks.

For identifying the emergence of various CDW states, optical-pumping-induced CDW diffraction pattern changes were monitored by alternating between the unpumped ($t=-10\text{ps}$) and pumped ($t=20\text{ps}$) states, as the optical fluence F was increased gradually. Fig. S3 shows an example of such pattern evolution over selected fluences using the 800 nm photons at a base temperature $T_B=150\text{K}$.

Further analysis based on the procedure described in Sec. S3 provides fluence-dependent CDW angle Φ and CDW suppression as depicted in Fig. S4, where the suppression ratio is calculated based on $[I_{CDW}(+20\text{ps}) - I_{CDW}(-10\text{ps})]/I_{CDW}(-10\text{ps})$. The boundary between different phases is characterized either by a step in the CDW angle Φ , or by the slope change of $\Phi(F)$ between two adjacent phases, depicted by the dashed lines in Fig. S4. Further information of these phase change

boundaries may also be seen in the dynamics where the transitions into various CDW states frequently produce a sequence of staircases as described in the main text. Based on the staircases, the critical conditions (Φ_c , A_c) can be determined for validating the conditions used to determine the phase boundaries in the fluence-dependent investigation. We later converted F into absorbed photon density, see discussion below. The results from different temperatures are combined as the basis for constructing the temperature-optical-density phase diagram (Fig. 4A).

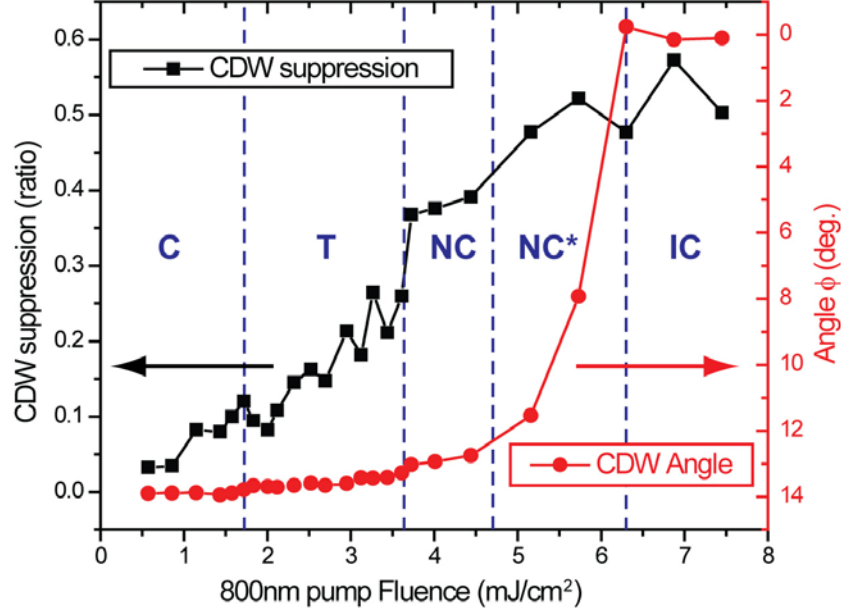


Fig. S4 The determination of CDW phase boundaries based on the presence of a step or a slope change.

5. CALCULATION OF ENERGY AND PHOTON DENSITY:

Whereas it is technically difficult to *in situ* monitor the absorption and reflectivity of the 1T-TaS₂ samples at highly quantitative levels due to their small sizes, it is easy to tell the difference between the two different pump wavelengths by visually inspecting the appearance of laser beam through the samples with an aperture. For sample thicknesses of 30-50 nm, in the case of the 800 nm photons it is strongly attenuated, whereas in the case of 2500nm, a significant portion of the intensity is transmitted. We extract the reflectivity R and the penetration depth δ of our single-crystal samples from the literature values based on the optical constant measurements [53]. We convert from temperature-dependent optical constants to determine the R and the δ values for the range of temperatures of our experiments.

Based on these values, we determine the absorbed energy density ΔH deposited into the sample in the following way:

$$\Delta H = \frac{F(1-R)(1-e^{-t/\delta})}{t}, \quad (\text{S1})$$

where F is the pump fluence on sample surface, R is the reflectivity, and t is sample thickness.

The sample thickness is characterized by zero-loss electron energy loss spectroscopy using a TEM (JEOL2200FS). For the specific sample chosen to construct the phase diagram, $t = 45\text{nm}$. We note that the sample thickness is near the penetration depth of the laser for the 800 nm case [30nm at both

room temperature (RT) and 150K]. This means that initially there was higher carrier density near the top surface. Nonetheless given that the phase diagram is determined at longer time (+20 ps), at which the carrier density is expected to equilibrate between different layers over the range of t , therefore the denominator in Eqn. (S1) is set to be t . In the case of 2500 nm excitation where δ is significantly larger than the sample thickness (100nm at RT, and 130nm at 150K), the carrier density is nearly homogeneous throughout the probed volume even at the earlier times. The reflectivity R for 800nm is 0.41 at RT and 0.45 at 150K; for 2500nm, R is 0.53 at RT and 0.58 at 150 K. These determinations are consistent with the values quoted in other literature which we compared with our measurements[19,40].

The absorbed photon density n_λ can be calculated as:

$$n_\lambda = \Delta H / h\nu , \quad (\text{S2})$$

where $h\nu$ is photon energy. This is under the assumption that each absorbed photon generates an electron-hole pair, namely without carrier multiplication effect.

Generally, carrier multiplication may occur under a high kinetic energy or driven by a high field. Since the applied optical field is in the range 1-10 kV/m, field-driven carrier multiplication may be ignored here. For the consideration of the kinetic effect, the initial carrier energy, K , is of the order of the excess energy Δ , namely $K \sim \Delta/2$. For the long wavelength photons (2500 nm), K ($\sim 0.1-0.2$ eV) is insufficient to generate additional electron-hole pairs. In the case of 800nm photons, it is a possibility if the scattering rate is sufficiently high. However, in TaS₂, the free carriers are strongly dressed by the polaronic effect. There, it is expected that carrier multiplication would be suppressed as compared to a rigid band system [54]. Nonlinear excitation may increase the carrier energy, however, nonlinear absorption is a minor channel in the range of optical fluences applied here. The lack of power-law dependent nonlinear growth in the trend of the fluence-dependent suppression of CDW, even under the 800nm optical excitation as depicted in Fig. S4 (black line), qualitatively affirms this argument.

For calculating the energy density absorbed by the samples to induce thermodynamic phase transitions from a base temperature (such as $T_B=150$ K in Fig. 2), in order to compare with optically induced transitions, we integrate the heat capacity C_V and latent heat H_L of 1T-TaS₂ crystals in these temperature ranges based on reference [36]:

$$\Delta H_{thermal} = \int_{T_B}^T C_V dt + H_L(T). \quad (\text{S3})$$